

## Vulnerability analysis of steel roofing cladding

Ji, X.; Huang, Guilan; Zhang, X.; Kopp, Gregory

DOI:

[10.1016/j.engstruct.2017.11.068](https://doi.org/10.1016/j.engstruct.2017.11.068)

License:

Creative Commons: Attribution-NonCommercial-NoDerivs (CC BY-NC-ND)

*Document Version*

Peer reviewed version

*Citation for published version (Harvard):*

Ji, X, Huang, G, Zhang, X & Kopp, G 2018, 'Vulnerability analysis of steel roofing cladding: influence of wind directionality', *Engineering Structures*, vol. 156, pp. 587-597. <https://doi.org/10.1016/j.engstruct.2017.11.068>

[Link to publication on Research at Birmingham portal](#)

### General rights

Unless a licence is specified above, all rights (including copyright and moral rights) in this document are retained by the authors and/or the copyright holders. The express permission of the copyright holder must be obtained for any use of this material other than for purposes permitted by law.

- Users may freely distribute the URL that is used to identify this publication.
- Users may download and/or print one copy of the publication from the University of Birmingham research portal for the purpose of private study or non-commercial research.
- User may use extracts from the document in line with the concept of 'fair dealing' under the Copyright, Designs and Patents Act 1988 (?)
- Users may not further distribute the material nor use it for the purposes of commercial gain.

Where a licence is displayed above, please note the terms and conditions of the licence govern your use of this document.

When citing, please reference the published version.

### Take down policy

While the University of Birmingham exercises care and attention in making items available there are rare occasions when an item has been uploaded in error or has been deemed to be commercially or otherwise sensitive.

If you believe that this is the case for this document, please contact [UBIRA@lists.bham.ac.uk](mailto:UBIRA@lists.bham.ac.uk) providing details and we will remove access to the work immediately and investigate.

1 **Vulnerability analysis of steel roofing cladding: influence of wind directionality**

2 Xiaowen Ji, Guoqing Huang, Xinxin Zhang, Gregory A. Kopp

3 Xiaowen Ji: S. M. ASCE; PhD Student, School of Civil Engineering, Southwest  
4 Jiaotong University, Chengdu, China 610031, [jixiaowen900308@gmail.com](mailto:jixiaowen900308@gmail.com)

5 Guoqing Huang (corresponding author): Professor, School of Civil Engineering,  
6 Southwest Jiaotong University, Chengdu, China 610031, [ghuang1001@gmail.com](mailto:ghuang1001@gmail.com)

7 Xinxin Zhang: Engineer, Berkshire Hathaway Specialty Insurance, Boston, MA, USA  
8 02110, [Xinxin.Zhang@bhspecialty.com](mailto:Xinxin.Zhang@bhspecialty.com)

9 Gregory A. Kopp: M. ASCE; Professor, Boundary Layer Wind Tunnel Laboratory,  
10 Faculty of Engineering, University of Western Ontario, London, ON, Canada  
11 N6A5B9, [gakopp@uwo.ca](mailto:gakopp@uwo.ca)

12 **Abstract**

13 Steel roofing is widely used for non-residential facilities. However, it is  
14 vulnerable to high winds. This paper addresses a damage estimation framework that  
15 incorporates wind loading correlation and wind directionality effects for steel roofing.  
16 In this framework, external pressures were measured from wind tunnel testing. At  
17 positions where pressure measurements are not available, a proper orthogonal  
18 decomposition (POD) method is introduced to interpolate external wind pressures.  
19 Internal pressures due to openings in the building envelope are taken into account by  
20 simulation. Then, the internal forces on fasteners distributed on the steel roof are  
21 evaluated by the influence surface method, with corresponding peak values estimated  
22 by a Gumbel conversion approach. Furthermore, the failure probability of a single

23 cladding element and the damage ratio for the whole roof are determined based on  
24 Monte Carlo simulation (MCS), where the correlation among internal forces of  
25 fasteners is incorporated by a Nataf transformation. Finally, wind directionality  
26 effects are integrated in order to provide a comprehensive damage assessment for the  
27 roofing. Although the proposed framework works for existing buildings, it may  
28 potentially benefit the performance-based design for new low-rise buildings.

29 **Keywords:** Wind damage estimation; Steel roofing; Proper orthogonal  
30 decomposition; Internal pressure; Correlation; Nataf transformation; Wind  
31 directionality

## 32 **1. Introduction**

33 Metal structures are widely used for low-rise buildings, especially for non-  
34 residential buildings. Based on the statistics from Metal Building Manufacturers  
35 Association (MBMA), approximately 65% of non-residential low-rise buildings are  
36 built with metal structures in USA (e.g., Dabral and Ewing 2009). Among these metal  
37 structures, lightweight steel structures represent a significant proportion and are  
38 popular for warehouses, sheds, airplane hangars and industrial buildings, which are  
39 vulnerable during hurricanes (or typhoons or tropical cyclones), thunderstorms and  
40 tornadoes (e.g., Perry et al. 1990; Ginger et al. 2007). For example, typhoon  
41 “Rananim” in 2004 devastated industrial buildings in Zhejiang Province, China,  
42 including collapsed area of 2.72 million m<sup>2</sup> and damaged area of 7.56 million m<sup>2</sup>  
43 (Song and Ou 2009).

44 Post-event damage surveys have indicated that the majority of damage to steel

45 structures is related to the breach of the envelope instead of the collapse of the main  
46 frame (NIST 2006). The breach of the roofing not only introduces losses to the  
47 building itself, but also triggers further damage to interior contents due to secondary  
48 perils, e.g., rain penetration. Additionally, business interruption increases indirect  
49 losses of income, which is a common concern for the insurance sector. Therefore, it is  
50 important to analyze and predict wind-induced damage for steel roofing in order to  
51 conduct damage mitigation and risk management assessments.

52       Damage analysis of low-rise buildings, especially wood-frame structures, under  
53 high winds has received significant attentions from the engineering community. Lee  
54 and Rosowsky (2005) assessed the wind-induced fragility of roof sheathing for light  
55 wood-frame structures. Li and Ellingwood (2006) proposed probabilistic risk  
56 assessment methods to evaluate performance and reliability of low-rise light-frame  
57 wood residential constructions in hurricane-prone region of the United States, where  
58 the importance of uncertainties is highlighted. Recently, aerodynamic databases have  
59 been applied to wind damage assessments. Zhao and Gu (2011) presented a database-  
60 assisted wind vulnerability assessment model for metal buildings. Huang et al. (2015)  
61 introduced a database-assisted probabilistic damage estimation approach for asphalt  
62 shingle roofing. Konthesingha et al. (2015) developed a vulnerability model for metal-  
63 clad industrial building in a tropical cyclone region. Huang et al. (2016) developed a  
64 damage estimation method for roof panels where the wind loading correlation was  
65 taken into account. In addition to structural component damage analyses, the wind-  
66 induced economic loss for metal roofing was discussed by Dabral and Ewing (2009).

67        Despite these achievements, there is a need to develop an integrated database-  
68        assisted approach to incorporate important factors such as wind loading correlation  
69        and wind directionality effects for the wind-induced damage analysis of low-rise  
70        building roof components. Cope et al. (2005) showed that the correlation of the  
71        surface pressures varies with direction and became strong under quartering winds and  
72        winds perpendicular to the roof gable. Huang et al. (2016) had found that the wind  
73        loading correlation may significantly influence the standard deviation (STD) of the  
74        damage ratio for roof panels. Although directionality effects have been widely  
75        recognized and incorporated in structural and cladding design, it has not yet been well  
76        addressed in vulnerability studies. Obviously, the wind damage of roof components  
77        will also depend on wind direction. To develop a comprehensive understanding of  
78        structural vulnerability, and for the sake of wind-induced damage mitigation and risk  
79        management, one needs to integrate the vulnerabilities of all directions with the local  
80        wind climate data within a framework that also considers wind load correlations and  
81        other influential factors.

82        Based on an illustrative low-rise building model whose wind pressure data were  
83        measured in a wind tunnel study, a wind damage estimation method incorporating the  
84        wind loading correlation and wind directionality for steel roofing is addressed in this  
85        paper. The paper is organized as follows. First, descriptions of the steel roofing and  
86        wind pressure data are introduced. Second, POD is adopted to interpolate the external  
87        wind pressure for roof locations where there are no pressure data. Third, the internal  
88        pressure is determined by simulation. Fourth, the internal forces on fasteners

89 distributed on the steel roof are computed with the aid of the influence-surface  
90 approach, with the corresponding peak internal forces estimated by a Gumbel  
91 conversion method. Fifth, the failure probability of a single panel and the damage  
92 ratio of whole roof are determined based on MCS, where the correlation among  
93 internal forces on fasteners is considered by a Nataf transformation. Sixth, the  
94 influence of wind directionality is incorporated in the damage estimation. In the end,  
95 concluding remarks are given.

## 96 **2. Descriptions of wind pressures and steel roofing**

97 The illustrative prototype industrial building used in this study has a full-scale  
98 size of 62.5 ft × 40 ft × 12 ft (19.05 m × 12.2 m × 3.66 m), a roof slope of 1:12, and is  
99 assumed to be located in suburban terrain. The wind pressure data were obtained from  
100 wind tunnel tests conducted at the University of Western Ontario (UWO), as reported  
101 by Ho et al. (2005), with significant comparisons to existing data provided by St.  
102 Pierre et al. (2005). The model scale was 1:100, with 335 taps distributed on the roof  
103 top. These are shown as blue dots in Figure 1. The sampling frequency was 500 Hz  
104 with a sampling time of 100 s. The tests were conducted in suburban terrain with  
105 roughness length of about 0.3 m, under a reference mean wind speed of 13.7 m/s at  
106 the equivalent of 10 m above the ground, which corresponds to a mean wind speed of  
107 6.1 m/s at the roof height (3.66 m). The tests were carried out at various wind angles  
108 of attack (AOAs) with intervals of 5° from 0° to 90° and from 270° to 360°. In the rest  
109 of paper, if without any specification, wind speeds are referred to 10-min mean wind  
110 speeds at the roof height.

111 There are many types of steel cladding profiles that are commonly used in  
112 construction, such as pierced-fixed and standing-seam steel cladding systems. Due to  
113 the requirements of large spans, low price, and simplicity of construction and also  
114 being well-researched (e.g., Mahaarachchi and Mahendran 2009), the high-strength  
115 trapezoidal steel cladding with closely spaced ribs is selected as the roof panel for this  
116 study. In the current study, the size of a single cladding panel is assumed to be 750  
117 mm  $\times$  6096 mm with a thickness of 0.6 mm. The height of crest is 35 mm and ribs are  
118 closely spaced with an interval of 125 mm between two neighboring crests. The  
119 layout of the cladding on the roof is shown in Figure 1 where 50 (2  $\times$  25) steel  
120 cladding panels are distributed on the roof. The cladding is made of high-strength  
121 steel G550 (yielding stress = 690 MPa). Self-tapping screws with head diameters of  
122 11 mm are assumed as the connection fasteners. Further details on this type of  
123 cladding can be found in Mahaarachchi and Mahendran (2009).

124 For the cladding cross section, four screws are used to connect the roof cladding  
125 to the purlins at alternate crests. Along the rib, four screws are also uniformly  
126 distributed. A schematic description can be found in Figures 2 (a) and (b). The  
127 locations of screws on a cladding panel are represented by the coordinate system  
128 shown in Figure 2 (a). For example, x<sub>2</sub>y<sub>3</sub> denotes the screw at the intersection of line  
129 x<sub>2</sub> and line y<sub>3</sub> on the panel. Two adjacent cladding panels overlap at marginal crests  
130 and share common screws, as shown in Figure 2 (c). The purlin spacing of the  
131 prototype building in Mahaarachchi and Mahendran (2009) is between 0.9 m and 1.1  
132 m. And in practice, the purlin spacing at the edge of the building is smaller to resist

133 larger wind pressures. For convenient illustration, the spacing has been adjusted to  
134 reduce the number of screws here.

### 135 **3. POD-based wind pressure interpolations**

136 To determine the wind-induced internal forces on a screw, ideally, the associated  
137 cladding panels should be assigned sufficient pressure taps in the wind tunnel  
138 experiment. However, not every panel satisfies this requirement, as shown in Figure  
139 1. It can be seen that, for many panels, there are no pressure taps. In order to evaluate  
140 the internal forces on the screws, ten proxy taps are evenly assigned along the central  
141 line of the each of the panels (see the red “+” in Figure 1). The pressures at these  
142 locations are interpolated from existing taps. Several interpolation techniques have  
143 been developed and applied for various purposes in database-assisted design (DAD),  
144 such as POD and artificial neural networks (ANN) (e.g., Tamura et al. 1997; Chen et  
145 al. 2002, 2004). Previous studies have shown that POD has good performance for  
146 wind-induced pressure interpolation (e.g., Bienkiewicz et al. 1993; Tamura et al.  
147 1997) and extrapolation (Chen et al. 2004). In the present study, POD will be used to  
148 reconstruct the wind pressure field on the low-rise building roof due to its adaptability  
149 and easy implementation. One advantage of POD is that it can characterize a  
150 multivariate process with a few modes.

151 If one assumes that  $\mathbf{C}_p(t) = \{C_{P_1}(t), C_{P_2}(t), \dots, C_{P_N}(t)\}^T$  is a zero-mean  $N$ -  
152 variate fluctuating wind pressure coefficient vector, where  $N$  is the number of taps in  
153 the wind tunnel testing, POD can be used to find a set of optimal orthonormal basis  
154 vectors  $\Theta = [\Theta_1, \Theta_2, \dots, \Theta_N]$  and  $\mathbf{C}_p(t)$  can be expanded as

155 
$$\mathbf{C}_p(t) = \mathbf{\Theta} \mathbf{a}(t) = \sum_{i=1}^N \Theta_i a_i(t) \quad (1)$$

156 where the component  $a_i(t)$  is the projection of  $\mathbf{C}_p(t)$  on the basis vector  $\Theta_i$ ,  
 157  $i = 1, 2, \dots, N$ . Note that the mean component has been removed as discussed by  
 158 Tamura et al. (1997). The basis vector set  $\mathbf{\Theta}$  can be determined from the eigenvalue  
 159 equation (Bienkiewicz et al. 1993)

160 
$$\mathbf{R}_p \mathbf{A} \mathbf{\Theta} = \mathbf{\Theta} \mathbf{\Lambda} \quad (2)$$

161 where  $\mathbf{R}_p$  is the covariance matrix of  $\mathbf{C}_p(t)$ ;  $\mathbf{A} = \text{diag}(A_1, A_2, \dots, A_N)$  and  $A_i$  is  
 162 the tributary area of the  $i$  th pressure tap;  $\mathbf{\Lambda} = \text{diag}(\lambda_1, \lambda_2, \dots, \lambda_N)$  is diagonal  
 163 matrix and  $\lambda_i$  is the  $i$  th eigenvalue. If the pressure taps are distributed uniformly and  
 164 tributary areas associated with different taps are identical, then Eq. (2) is rewritten as

165 
$$\mathbf{R}_p \mathbf{\Theta} = \mathbf{\Theta} \mathbf{\Lambda}^\# \quad (3)$$

166 where  $\mathbf{\Lambda}^\# = \text{diag}(\frac{\lambda_1}{A}, \frac{\lambda_2}{A}, \dots, \frac{\lambda_N}{A})$  and  $A$  is the tributary area. If the pressure taps  
 167 are distributed non-uniformly, Eq. (2) can be pre-multiplied by  $\mathbf{A}^{1/2}$  and an  
 168 equivalent form is given as (Jeong et al. 2000)

169 
$$\mathbf{R}_p^* \mathbf{\Theta}^* = \mathbf{\Theta}^* \mathbf{\Lambda} \quad (4)$$

170 where  $\mathbf{R}_p^* = \mathbf{A}^{1/2} \mathbf{R}_p \mathbf{A}^{1/2}$  and  $\mathbf{\Theta}^* = \mathbf{A}^{1/2} \mathbf{\Theta}$ . Note that the modification guarantees that  
 171 the transformed  $\mathbf{R}_p^*$  is a real and symmetric matrix, and allows the Cholesky  
 172 decomposition. The target orthogonal basis vector then can be obtained through the  
 173 inverse transformation

174 
$$\mathbf{\Theta} = \mathbf{A}^{-1/2} \mathbf{\Theta}^* \quad (5)$$

175 It is clear that the eigenvalue matrix  $\mathbf{\Lambda}$  is unchanged in the transformation.

176        Once the value of the basis vector for the proxy tap is estimated by the spatial  
177 interpolation, the fluctuation of the wind pressure at this tap can be interpolated from  
178 non-uniformly distributed taps. In this study, the first 300 modes are applied to  
179 reconstruct the wind pressure time histories. The interpolated fluctuation of the wind  
180 pressure coefficient at an existing tap (highlighted by a circle in Figure 2) is compared  
181 with the measured counterpart in Figure 3. Consistency can be found in time histories  
182 and lower frequency part of power spectral densities (PSDs). Similar results can be  
183 found for other taps. Figure 4 shows the interpolated fluctuating pressure coefficient  
184 at a proxy tap (highlighted by a rectangle in Figure 1). By the spatial interpolation, the  
185 mean component of the wind pressure coefficients at the proxy taps is obtained.

#### 186 **4. Incorporation of internal pressures**

187        Internal pressure appears because of the leakage or openings of a building in  
188 response to external wind pressures. Because internal pressure has a significant  
189 influence on the structural cladding system, it has been investigated by many scholars  
190 (e.g., Holmes 1979; Oh et al. 2007). Previous studies showed that internal pressure is  
191 affected by various factors, such as local external pressure, opening size, building  
192 volume and flexibility of building envelope (e.g., Oh et al. 2007). Based on the work  
193 by Holmes (1979), Oh et al. (2007) showed that simulation of internal pressure time  
194 histories for buildings with a dominant opening and/or small leakage in the walls can  
195 be accurately simulated using external wind pressures, such as those from the  
196 database of Ho et al. (2005), as input.

197        Clearly, internal pressures are dependent on the damage state of the building

198 envelope and cladding. In reality, the wind-induced damage on the building envelope  
199 and cladding is a progressive process and the determination of internal pressure is  
200 challenging in that additional wind tunnel experiments are usually required. To  
201 simplify the damage process, in this study, buildings under high winds are assumed to  
202 undergo the following three stages. Stage 1: Enclosed building. In the beginning, the  
203 building is nominally sealed with background leakage. In this case, the internal  
204 pressure is usually negative (i.e., suction) and increases the load on the windward wall  
205 and reduces the wind load on the roof. Stage 2: Partially-enclosed building. The wall,  
206 especially a door or window, may be broken due to wind-borne debris-impacts or  
207 larger net pressure loads. Loss of these components causes a dominant opening on the  
208 wall and makes the building partially enclosed. At this stage, the internal pressure  
209 usually becomes positive, which leads to an increase of the net wind loads on the roof  
210 and makes roof cladding more vulnerable to wind. Stage 3: Roof cladding loss or  
211 component failures. At this stage, portions of the roof panels may be removed,  
212 causing new openings on the roof. Accordingly, the internal pressure may decrease, to  
213 some extent. Because the roof cladding tends to be most vulnerable at the second  
214 stage, partially-enclosed buildings are studied herein. The related internal pressure can  
215 be obtained by either wind tunnel tests (such as the UWO data) or via simulation, with  
216 similar accuracy (Oh et al. 2007). In this study, the latter will be adopted. In addition,  
217 the internal pressure in the third stage is assumed to be unchanged, which may be  
218 conservative for the cladding damage estimation. Although the wind damage of a  
219 building is also sensitive to its construction and the cladding system details, this study

220 focuses on the damage to the roof system conditioned on a given construction and  
221 cladding system.

222 For a single opening in the wall, the governing equation for determining the  
223 internal pressure within the building volume is obtained from the unsteady form of the  
224 Bernoulli equation (for a recent derivation, see Oh and Kopp 2014). This equation,  
225 which represents the conservation of energy of the flow through the opening, is (e.g.,  
226 Holmes 1979; Holmes and Ginger 2012):

$$227 \quad \frac{\rho l_e V}{\gamma a P_0} \ddot{C}_{pi} + \left[ \frac{\rho V \bar{U}_h}{2 \kappa \gamma a P_0} \right]^2 \dot{C}_{pi} |\dot{C}_{pi}| + C_{pi} = C_{pe} \quad (6)$$

228 where  $\rho$  is the air density;  $l_e$  is the effective length of an “air slug”;  $V$  is the internal  
229 volume;  $\gamma$  is the ratio of specific heat capacities of air;  $a$  is the opening area;  $P_0$  is the  
230 atmospheric pressure;  $\bar{U}_h$  is the mean wind speed at reference height;  $\kappa$  is the  
231 discharge coefficient compensating for various energy losses;  $C_{pe}$  and  $C_{pi}$  denote the  
232 external and internal pressure coefficient, respectively. According to Vickery and  
233 Bloxham (1992), in the present study,  $l_e = \sqrt{a\pi}/2$  and  $\kappa = 0.6$  will be adopted. It  
234 should be mentioned that the effects of friction losses are not incorporated here.  
235 However, it must be considered for narrow and long openings. Because Eq. (6) has  
236 the form of a spring-mass-damper system, the internal pressure has a natural  
237 frequency that is known as the Helmholtz frequency,  $\frac{1}{2\pi} \sqrt{\frac{\kappa \gamma a P_0}{\rho l_e V}}$ , which is the  
238 resonant frequency of the internal pressures (e.g., Holmes 1979; Oh et al. 2007).

239 Similar to Oh et al. (2007), a rectangular dominant opening is assumed on front  
240 wall under AOA of  $270^\circ$  (see Figure 1). The ratio of the opening area to the wall area

241 is assumed to be 3.2%, while the building porosity is considered to be negligibly  
242 small for the current study. While the current study is illustrative, neglecting the  
243 leakage should be reasonable for the damage estimation when one considers the other  
244 uncertainties. A 4<sup>th</sup>-order Runge-Kutta method can be used to solve the above  
245 nonlinear differential equation. Note that the opening is assumed to appear on front  
246 wall instead of side walls. That is, for AOAs from 180°-360°, the opening is same to  
247 that for AOA of 270°, and for AOAs from 0°-180°, it is symmetrical to that for AOA  
248 of 270°.

249 For mean wind speed of 37 m/s and AOA of 315°, the simulated internal pressure  
250  $C_{pi}$  is presented together with a corresponding external pressure  $C_{pe}$  in Figure 5 (a).  
251 Here, 37 m/s is used for illustrative purposes and is representative of a magnitude  
252 where damage may be observed. It can be seen internal pressures are almost  
253 coincident with the external wall pressures for this particular case with the amplitude  
254 of the internal pressures being slightly larger than that of the external pressure due to  
255 the Helmholtz resonance. PSD functions are also given in Figure 5 (b). The peak in  
256 PSD of  $C_{pi}$  is the Helmholtz frequency, which is 2.4 Hz in full scale. Together with  
257 (interpolated) external pressures on the roof, the simulated internal pressure will be  
258 used to estimate the net wind load on the cladding.

## 259 **5. Determination of internal forces and their peaks on screws**

260 High winds can cause large uplift forces on roof cladding, and these forces will  
261 be transferred to the self-tapping screw fasteners. As a consequence, dimpling around  
262 a screw arises initially and cracks appear. Eventually, the steel cladding will be pulled

263 through the screw connection (i.e., pull-through failure). It should be noted that for  
264 cladding systems on metal buildings, failures due to low-cycle fatigue (e.g.,  
265 Mahendran 1990; Xu 1995, 1997; Henderson and Ginger 2011) are not considered in  
266 the current methodology and analysis; rather, failures mainly due to stress  
267 concentrations or internal forces in the screws are considered in the development of  
268 the method. In this section, an influence-surface-based approach is used to calculate  
269 internal (i.e., tension due to uplift) forces on screws, firstly. Then the peak value  
270 distributions are estimated via a Gumbel conversion method.

271 To estimate the internal forces on screws, a direct way is to perform the finite  
272 element (FE) analysis for all claddings and screws. However, such an analysis needs  
273 significant computational time. According to Mahaarachchi and Mahendran (2009),  
274 the internal forces of screws on any cladding panel can be estimated individually on a  
275 single- or half-cladding-panel basis. In this study, to improve the calculation  
276 efficiency, the (linear) influence coefficient approach is used to estimate the internal  
277 forces on a screw (e.g., Henderson 2010; Kopp 2013). Accordingly, the internal force  
278 of a screw can be obtained as follows

$$279 \quad X(t) = \iint q(x, y, t) I_c(x, y) dx dy \quad (7)$$

280 where  $I_c(x, y)$  is the internal-force, influence coefficient at position  $(x, y)$ ;  $q(x, y, t)$   
281 is the corresponding net pressure (summation of the external and internal pressures).  
282 Because the layout of screws is the same for all cladding sheets and each cladding  
283 sheet is bi-symmetric, only the internal force influence coefficients for 4 screws are  
284 needed. For illustration, an influence surface for the internal force on screw x2y3 is

285 given in Figure 6 where the vertical axis represents the influence coefficient. It reveals  
286 that the internal force is mainly due to the pressure near the crest, where the screw is  
287 located. Compared with the aforementioned, direct approach, the influence-surface-  
288 based approach is efficient for the determination of internal forces on screws.

289 Usually, the duration of a pressure time history of wind pressure from a wind  
290 tunnel is 20 to 60 min in full scale. The same length is applied to the internal forces on  
291 the screw. Hence, the traditional block maximum method is not applicable in the  
292 evaluation of the probability density function (PDF) of the peak internal force during  
293 the interval of 10 min or 1 h. However, if the peak value distribution of the sample  
294 approaches the Gumbel distribution, a Gumbel conversion method, which was  
295 introduced by Cook and Mayne (1980), can project Gumbel parameters for a given  
296 longer interval based on those determined from a shorter interval. Numerous  
297 experimental results have validated the appropriateness of the Gumbel distribution in  
298 modeling the peak wind pressure (e.g., Cook and Mayne 1980; Holmes and Cochran  
299 2003). Peng et al. (2014) applied this method to project Gumbel parameters for a 15-  
300 min duration using those determined from 15 segments of 1-min duration and  
301 illustrated that the conversion method performed well for wind pressure peak  
302 prediction. The conversion method is appropriate to estimate PDFs of peak internal  
303 forces for hundreds of screws due to its relative simplicity, accuracy and efficiency.

304 Let  $W_{T_1}$  denote the peak value of the internal force process over  $T_1$  min, say, 1  
305 min. Suppose  $W_{T_1}$  follows Gumbel distribution, i.e.,

306 
$$\Psi_{W_{T_1}}(w) = \exp\{-\exp[-\alpha_{w_{T_1}}(w - \hat{w}_{T_1})]\}$$
 (8)

307 where the mode  $\widehat{w}_{T_1}$  is the most likely value and  $1/\alpha_{w_{T_1}}$  is the dispersion. If the  
 308 cumulative distribution function (CDF) of the peak value  $W$  over  $T$  min, say, 10 min  
 309 or 1 h, is given as

$$310 \quad \Psi_W(w) = \exp\{-\exp[-\alpha_w(w - \widehat{w})]\} \quad (9)$$

311 If peak values from different subsamples over  $T_1$  min are mutually independent, then  
 312 the peak value distribution over  $T$  min can be computed as (e.g., Cook and Mayne  
 313 1980; Huang 2008)

$$314 \quad \Psi_W(w) = [\Psi_{w_{T_1}}(w)]^{T/T_1} = \exp\{-\exp[-\alpha_{w_{T_1}}(w - \widehat{w}_{T_1}) + \ln(T/T_1)]\} \quad (10)$$

315 The mode and dispersion parameters are given as

$$316 \quad \widehat{w} = \widehat{w}_{T_1} + \ln(T/T_1)/\alpha_{w_{T_1}}; \quad \alpha_w = \alpha_{w_{T_1}} \quad (11)$$

317 The product  $\Pi_w = \alpha_w \widehat{w}$  is a dimensionless characteristic product.

318 In this paper, the internal force time history is divided into subsamples with  
 319 intervals of 1 min, under various mean wind speeds. For instance, the number of  
 320 subsamples is about 27, for a wind speed of 37 m/s. Although  $T_1 = 1$  min has been  
 321 used for wind pressure data by Peng et al. (2014) and Gavanski et al. (2016), the  
 322 independence of peak internal forces over 1 min shall be examined here. The internal  
 323 force at screw x2y2 on Cladding A under AOA of  $315^\circ$  is selected as the example.  
 324 Under the mean wind speed equal to 25, 37 and 49 m/s at roof height, the associated  
 325 autocorrelation functions are shown in Figure 7 where the time lag is in the full-scale  
 326 dimensions. It can be seen that the autocorrelation coefficients drop below 0.2 after 5,  
 327 3 and 2.5 s under mean wind speeds of 25, 37 and 49 m/s, respectively. This is a good  
 328 indication of independence between any two peak values separated by more than 5

329 seconds. Similar results can be found for other screws. Hence, peak values of internal  
330 forces over 1 min can be reasonably assumed to be independent. Under such an  
331 assumption, peak values from subsamples are fitted by Gumbel distribution. Then, the  
332 CDF of peak values over 1 min is converted to that over 10 min via Eqs. (10) and  
333 (11).

## 334 **6. Consideration of correlation for peak internal forces**

335 Cope et al. (2005) illustrated that the high correlations of the surface pressures  
336 are induced by quartering winds and winds perpendicular to the roof gable.  
337 Subsequently, highly correlated wind pressures may lead to high correlations among  
338 internal forces on screws. Huang et al. (2016) showed that highly correlated pressures  
339 could cause larger variation of the damage ratio, or higher risk for roof components.  
340 Hence, the correlation among the peak internal forces should be considered for  
341 estimates of the wind-induced damage on steel cladding. However, it is difficult to  
342 determine the correlation for peak values over 10 min directly using the current UWO  
343 data, which is of limited length (around 20~40 min in the full scale).

344 To make the proposed framework feasible, an alternative to approximately  
345 estimate the correlation for peak internal forces over 10 min will be introduced. In this  
346 alternative, the relationship for the correlations of peak internal forces over 1 min and  
347 10 min is assumed to be equivalent to that for peak wind pressures, which will be  
348 estimated from a set of very long wind pressure data. The derivation is presented in  
349 the Appendix. Then, the correlation for peak values over 10 min can be approximately  
350 estimated from that for peak values over 1 min. To incorporate the correlation among

351 peak internal forces in the cladding damage estimation, the Nataf transformation is  
 352 adopted (e.g., Liu and Der Kiureghian 1986), which relates correlated non-Gaussian  
 353 variables to correlated Gaussian counterparts.

354 Assume a random variable vector with components made up of the peak internal  
 355 forces on screws such that  $\mathbf{W} = [W_1, W_2, \dots, W_n]^T$  whose marginal CDF is  
 356  $F_{W_j}(w_j)$ ,  $j = 1, 2, \dots, n$  and  $n$  is the number of screws. This vector can be  
 357 transformed to its corresponding standard Gaussian random vector  
 358  $\mathbf{Z} = [Z_1, Z_2, \dots, Z_n]^T$  by

$$359 \quad Z_j = \Phi^{-1}[F_{W_j}(w_j)], \quad j = 1, 2, \dots, n \quad (12)$$

360 where  $\Phi(\cdot)$  denotes the standard Gaussian CDF. The Nataf transformation can be  
 361 derived as (e.g., Huang et al. 2016)

$$362 \quad f_{\mathbf{W}}(\mathbf{w}) = f_{W_1}(w_1)f_{W_2}(w_2)\cdots f_{W_n}(w_n) \frac{\varphi_n(\mathbf{z}, \mathbf{R}_{\mathbf{Z}})}{\varphi(z_1)\varphi(z_2)\cdots\varphi(z_n)} \quad (13)$$

363 where  $f_{\mathbf{W}}(\mathbf{w})$  is the joint PDF of peak internal forces and  $\varphi_n(\mathbf{z}, \mathbf{R}_{\mathbf{Z}})$  is the standard  
 364 Gaussian  $n$ -variate joint PDF with the correlation matrix  $\mathbf{R}_{\mathbf{Z}}$ .

365 With known  $\rho_{jk}^w$ , the correlation coefficient between  $W_j$  and  $W_k$ , can be  
 366 expressed as

$$367 \quad \rho_{jk}^w = \int_{-\infty}^{\infty} \int_{-\infty}^{\infty} \left( \frac{w_j - \mu_j}{\sigma_j} \right) \left( \frac{w_k - \mu_k}{\sigma_k} \right) \varphi_2(z_j, z_k, \rho_{jk}^z) dz_j dz_k \quad (14)$$

368 where  $\mu_j$  and  $\sigma_j$  are the mean and STD of  $W_j$ , respectively; and  $\rho_{jk}^z$  (correlation  
 369 coefficient between  $Z_j$  and  $Z_k$ ) is an element in  $\mathbf{R}_{\mathbf{Z}}$ . An important lemma is that  $\rho_{jk}^w$   
 370 is a strictly monotonic function with respect to  $\rho_{jk}^z$  (Liu and Der Kiureghian, 1986).  
 371 This leads to one-to-one mapping between  $\rho_{jk}^w$  and  $\rho_{jk}^z$ . To avoid iteration in above

372 equation, a series of empirical formulae were fitted by Liu and Der Kiureghian  
 373 (1986). If  $W_j$  and  $W_k$  both follow Gumbel distribution, Eq. (14) can be approximated  
 374 as

$$375 \quad \rho_{jk}^z = 1.064\rho_{jk}^w - 0.069(\rho_{jk}^w)^2 + 0.005(\rho_{jk}^w)^3 \quad (15)$$

376 Obviously, both the marginal CDF and correlation of the non-Gaussian variables are  
 377 maintained under the Nataf transformation.

## 378 7. Damage estimation of steel roofing

### 379 7.1 Failure probability and damage ratio of a roof cladding

380 Based on a comprehensive parametric study for the pull-through failures of the  
 381 trapezoidal steel cladding at the screw connections, Mahaarachchi and Mahendran  
 382 (2009) developed strength formulae for trapezoidal steel claddings with closed space  
 383 ribs. When G550 steel is used, the mean of the strength  $R$  is given as

$$384 \quad \mu_R = 0.04 \times \left( 4.7 - \frac{20f_y d_h}{Et} \right)^2 \left( \frac{h_c}{h_p} \right)^{3/4} \left( \frac{W_t}{W_c} \right)^{1/5} \left( 12 + \frac{1500t^2}{Ld_h} \right)^{1/3} d_h t f_y \quad (16)$$

385 where the steel yield stress  $f_y = 690$  MPa; the diameter of screw head  $d_h = 11$  mm;  
 386 the Young's modulus  $E = 200$  GPa; the cladding crest height  $h_c = 35$  mm; the crest  
 387 pitch  $h_p = 125$  mm; the cladding trough width  $W_t = 81.5$  mm; the cladding crest  
 388 width  $W_c = 43.5$  mm; the cladding thickness  $t = 0.6$  mm and the span between  
 389 purlins  $L = 1981.2$  mm. The coefficient of variation (the ratio of the STD to the  
 390 mean) is 0.12. The cladding strength  $R$  is assumed to follow Gaussian distribution, in  
 391 the current case, with mean of 2.15 kN and STD of 0.26.

392 Once the peak internal force on the screw is larger than the cladding strength  
 393 around the screw, the cladding may suffer from the pull-through failure. Due to the

394 lack of the research and experimental data, the peak internal force and the cladding  
 395 strength around a screw are regarded to be independent. The failure probability of  
 396 cladding around a screw is given by

$$397 \quad s = \iint_{r \leq w} f_R(r) f_W(w) dr dw \quad (17)$$

398 where  $f_R(r)$  is PDF of the cladding strength around the screw.

399 Previous investigations showed that 90% wind load would be redistributed to  
 400 two adjacent screws on the same crest if a screw fails to take the load (Henderson  
 401 2010; Konthesingha et al. 2015). As a consequence, internal forces on these two  
 402 screws will significantly increase, and the redistributed internal force may exceed the  
 403 cladding strength and the corresponding cladding sheet will very likely undergo  
 404 failure. Hence, it is appropriate to assume that the failure of one of the screws on a  
 405 cladding panel leads to the failure of the whole panel.

406 Apparently, the failure probability of a cladding panel is determined by the peak  
 407 internal forces and resistances at the screws on that cladding. The failure probability  
 408 can be expressed as

$$409 \quad p = 1 - \iint_{w_1 < r_1} \iint_{w_2 < r_2} \cdots \iint_{w_{n_s} < r_{n_s}} f_R(\mathbf{r}) f_W(\mathbf{w}) dr dw \quad (18)$$

410 where  $f_R(\mathbf{r})$  is the joint Gaussian PDF of strengths and can be determined based on  
 411 the assumption of independence. Note that  $f_W(\mathbf{w})$ , which is defined in section 6, has  
 412 incorporated the correlation among peak internal forces. In this study, the number of  
 413 screws,  $n_s$ , is 8 due to the symmetric layout of screws.

414 Suppose the number of cladding panels over the entire roof is  $N_C$ . To estimate

415 the overall damage of claddings over the roof, the damage ratio is used. It describes  
416 the extent of damage on the roof cladding and is defined as the percentage of total  
417 failed panels, i.e.,

$$418 \quad D = M_C / N_C \quad (19)$$

419 where  $M_C$  is the failed cladding number, and  $M_C$  and  $D$  are random variables.

## 420 **7.2 Monte Carlo simulation**

421 It is time-consuming to evaluate Eqs. (18) and (19) by a numerical method  
422 because they depend on several parameters including peak internal forces and  
423 strengths around screws, and their correlations. MCS is more efficient than a  
424 numerical method in estimating the damage ratio over the entire roof as well as the  
425 failure probability for each single cladding. It should be noted that the internal forces  
426 on many pairs of screws will be fully correlated. For example, the internal forces on  
427 screws x2y2 and x2y3 on a cladding are identical. One of two fully correlated forces  
428 in the simulation is taken out and the simulated force can be adopted for both.

429 Assume MCS is repeated for  $n_t$  rounds. In the  $m$  th simulation, the correlated  
430 peak internal forces at all screws are simulated via the Nataf transformation, firstly.  
431 The peak internal forces at all screws can be simulated in the following way. The  
432 correlated Gaussian vector  $\mathbf{Z}$  is simulated according to

$$433 \quad \mathbf{R}_Z = \mathbf{L}\mathbf{L}^T ; \mathbf{Z} = \mathbf{L}^{-1}\mathbf{U} \quad (20)$$

434 where  $\mathbf{U}$  is the independent standard Gaussian vector and the lower triangular matrix  
435  $\mathbf{L}$  shall be obtained by Cholesky decomposition of  $\mathbf{R}_Z$ . Once the sample of Gaussian  
436 vector  $\mathbf{Z}$  is generated, that of the non-Gaussian vector  $\mathbf{W}$  can be simulated

437 accordingly. Further details can be found in Huang et al. (2016).

438 In addition, Cholesky decomposition for matrix  $\mathbf{R}_Z$  may be not applicable  
439 because negative eigenvalues may still exist. These negative values appear due to  
440 highly correlated forces on different screws and/or computational errors. To solve this  
441 difficulty, the  $\mathbf{R}_Z$  matrix should be manipulated. First, this matrix can be written as

$$442 \quad \mathbf{R}_Z = \mathbf{V}^T \mathbf{\Omega} \mathbf{V} \quad (21)$$

443 where  $\mathbf{V}$  is the eigenvector matrix and  $\mathbf{\Omega}$  is the diagonal eigenvalue matrix. The  
444 negative eigenvalue in matrix  $\mathbf{\Omega}$  can be replaced by a small positive value such as  
445 0.001 in order to make the Cholesky decomposition available. Results show that the  
446 simulation is not sensitive to the minor changes in the eigenvalues. After the  
447 correlated peak internal forces have simulated, the independent resistances associated  
448 with those internal forces are generated accordingly. Note that the correlation of  
449 resistances is neglected due to a lack of available data.

450 Let  $f_{l,m}$  denote whether the  $l$  th cladding has failed in the  $m$  th simulation such  
451 that  $f_{l,m} = 0$  or 1 for undamaged or damaged, respectively. The failure probability of  
452 the  $l$  th cladding is

$$453 \quad p_l = \frac{1}{n_l} \sum_{m=1}^{n_l} f_{l,m} \quad (22)$$

454 where  $\sum_{m=1}^{n_l} f_{l,m}$  is the number of the failure for the  $l$  th cladding in the simulations. The  
455 damage ratio for  $m$  th simulation is given by

$$456 \quad d_m = \frac{1}{N_C} \sum_{l=1}^{N_C} f_{l,m} \quad (23)$$

457 where  $\sum_{l=1}^{N_c} f_{l,m}$  is the number of failed cladding panels in the  $m$  th simulation.

458 According to discussions by Huang et al. (2016), the random variable  $D$  will approach  
459 the Gaussian distribution approximately. The mean and STD of damage ratio are  
460 determined as

$$461 \quad \mu_D = \frac{1}{n_t} \sum_{m=1}^{n_t} d_m ; \quad \sigma_D = \sqrt{\frac{1}{n_t} \sum_{m=1}^{n_t} (d_m - \mu_D)^2} \quad (24)$$

### 462 7.3 Results and discussions

463 In the following discussions, the correlation for peak values over 10 min will be  
464 denoted as  $C_{10min}$ . For comparison, another three types of correlations will be also  
465 used to investigate the influence of the correlation of peak internal forces: the  
466 correlation for the parent process (denoted by  $C_{par}$ ), the correlation for peak values  
467 over 1 min (denoted by  $C_{1min}$ ), and no correlation (denoted by  $C_0$ ). Note that  $C_{par}$  and  
468  $C_{1min}$  are estimated based on the limited data, and  $C_{10min}$  is approximately estimated  
469 from  $C_{1min}$ .

470 Table 1 shows the correlation coefficients for internal forces on selected screws  
471 under mean wind speed of 37 m/s at roof height and AOA of 315° (The corresponding  
472 cladding numbers are marked in Figure 1). It can be observed that the correlation  
473 coefficients decrease from  $C_{par}$  to  $C_{1min}$  and further  $C_{10min}$ , which is consistent with the  
474 results in Luo and Huang (2016). Also, strong correlations can be found even for the  
475 distant screws. For example, the correlation coefficients between x2y2 on Cladding A  
476 and x2y3 on Cladding D are estimated as 0.917, 0.877 and 0.760 for  $C_{par}$ ,  $C_{1min}$  and  
477  $C_{10min}$ , respectively.

478 In total, 10,000 rounds of simulations are conducted based on  $C_{par}$ ,  $C_{1min}$ ,  $C_{10min}$   
479 and  $C_0$ , respectively. Once the peak internal forces and resistances at all screws are  
480 simulated, the failures for all screws can be judged and corresponding failure  
481 probabilities can then be estimated by the simulation. Failure probabilities can be  
482 evaluated numerically from Eq. (17). It should be pointed out that the correlation of  
483 peak internal force has no influence on screw failures. The contour map for the failure  
484 probabilities of all 608 screws under the mean wind speed of 37 m/s at roof height and  
485 AOA of  $315^\circ$  is shown in Figure 8. It can be seen that screws close to the leading  
486 edges are more vulnerable. It is also seen that screws along the line x2 (e.g., x2y3) on  
487 a cladding panel have larger failure probabilities, which indicates cladding failure  
488 possibly starts from these positions. This is attributed to the facts that these screws  
489 have relatively larger tributary areas and suffer from relatively larger wind loading.

490 Subsequently, failure probabilities of all cladding panels can be obtained. From  
491 Eq. (18), the correlation of peak internal forces will affect these probabilities. Results  
492 show that  $C_{par}$ ,  $C_{1min}$ ,  $C_{10min}$  and  $C_0$  have little effect on the failure probability of a  
493 cladding. With  $C_{10min}$  for illustration, failure probabilities of all cladding under mean  
494 wind speeds of 33, 37 and 41 m/s and AOAs of  $270^\circ$ ,  $315^\circ$  and  $360^\circ$  are shown in  
495 Figure 9. Here, the progressive damage can be observed. With the increase of the  
496 mean wind speed, the breach will spread from the windward side to leeward side  
497 under AOA of  $270^\circ$ , and start from the windward corner and spread radially to the  
498 leeward corner under  $315^\circ$ , and gradually extend from one edge to another one under  
499  $360^\circ$ . It can also be seen that the roof faces the highest risk for  $270^\circ$ ; not for  $315^\circ$ . This

500 observation can be explained as follows. Typically, the roof damage associated with  
501 AOA of  $315^\circ$  is expected to be largest due to the existence of the conical vortex if  
502 only the external pressures are considered. However, when a breakage on a windward  
503 wall is assumed, the internal pressure has a significant influence on the roof damage.  
504 In current study, the internal pressure under AOA of  $270^\circ$  on Stage 2 makes the roof  
505 most vulnerable.

506 The means and STDs of the damage ratios for  $C_{par}$ ,  $C_{1min}$ ,  $C_{10min}$  and  $C_0$  under  
507 various mean wind speeds and AOAs are plotted in Figure 10. Results show that the  
508 correlation has a negligible effect on the mean damage ratio. This is similar to results  
509 reported by Huang et al. (2016), where the wind loading correlation has no effect on  
510 the mean damage ratio for the roof panels. However, the STD may be sensitive to the  
511 correlation, i.e., it becomes larger with the increase of the correlation. For example,  
512 under mean wind speed of 37 m/s and AOA of  $315^\circ$ , the STDs of the damage ratio are  
513 about 0.147, 0.141 and 0.132 for  $C_{par}$ ,  $C_{1min}$  and  $C_{10min}$ , and that for  $C_0$  drops to less  
514 than 0.045. This is attributed to the fact that higher correlations among internal forces  
515 on screws cause the failures at different cladding panels more likely. Especially, if the  
516 wind loading correlations approach unit, those claddings may either fail or survive  
517 together, which will greatly increase the variation of damage ratio. Figure 11 shows  
518 the CDFs of the damage ratios for  $C_{par}$ ,  $C_{1min}$ ,  $C_{10min}$  and  $C_0$  under mean wind speed of  
519 37 m/s and AOA of  $315^\circ$ . It can be seen that the CDFs for first three correlations are  
520 almost identical, indicating correlations for parent process of internal forces, peak  
521 internal forces over 1 min and 10 min have similar effects on the distribution of

522 damage ratio. Besides, the consideration of correlation (e.g.,  $C_{par}$ ,  $C_{1min}$  and  $C_{10min}$ )  
523 may increase the variation of damage ratio, which may lead to the building in higher  
524 risks.

## 525 **8. Directionality in damage estimation**

526 The evaluation of directionality effect is critically important because of the  
527 coupling of building orientation and directional wind distribution. A given structure  
528 and its components respond differently to the wind of the same magnitude but  
529 different AOAs given all other conditions being equal. Also, wind speed distributions  
530 are different in each distribution due to the nature of macro- and micro-meteorological  
531 effects, e.g., effects from large scale wind climate and local terrain features. The  
532 ignorance of such effect would result in inaccurate predictions. While the effect of  
533 wind directionality on probabilistic estimation of wind load effects of structures has  
534 drawn significant attentions for load design purpose (e.g., Simiu and Scanlan 1996;  
535 Laboy-Rodrigues et al 2014; Zhang and Chen 2015), its study in vulnerability analysis  
536 has been limited in the literature. For example, ASCE 7-10 specifies a directionality  
537 reduction factor of 0.85 for the structural design of roofs and claddings (ASCE 2010).  
538 However, the directionality effect on vulnerability, i.e., damage status of a building  
539 altered by the directionality effect of the actual building aerodynamics (determined  
540 via the wind tunnel study), has rarely been considered as a separate parameter in  
541 previous literatures.

542 The consideration of directionality effects is also important since the wind  
543 climate for a prescribed location is unique and will introduce directionality, i.e., there

544 may be a dominant direction for winds in terms of both the frequency and magnitude.  
545 The overall vulnerability for a particular building at a particular location should be an  
546 integration of the vulnerabilities conditioned on prescribed directions, over all  
547 directions. Thus, the following discussions focus on a fully probabilistic method that  
548 considers the wind directionality, directional wind speed correlations as well as  
549 uncertainties in the damage ratio within a unified framework.

550 In this study, the historical wind speed record from Baltimore International  
551 Airport was used. The record was extracted from Automated Surface Observation  
552 System (ASOS) database operated by National Oceanic and Atmospheric  
553 Administration (NOAA) (<ftp://ftp.ncdc.noaa.gov/pub/data/asos-onemin/>). The original  
554 2-min mean wind speeds at 10-m height were converted to 10-min mean wind speed  
555 at the roof height of the building adopted in this paper. Wind speeds covering 360  
556 degrees are categorized into eight representative sectors with each denoted by their  
557 central directions  $\alpha_i = 45^\circ, 90^\circ, \dots, 360^\circ$  ( $i = 1, 2, \dots, 8$  indicates directions NE,  
558 E,  $\dots$ , N, respectively, as shown in Figure 12). Monthly maximum wind speed data  
559 are selected in each sector. In total, 156 monthly (from 2000 Jan to 2013 Dec)  
560 maxima are collected for every sector. In the following discussion, the damage  
561 analysis of steel cladding is performed with the consideration of the wind loading  
562 correlation among the screw peak forces over 10 min (i.e.,  $C_{10min}$ ).

### 563 **8.1 Without consideration of variation of damage ratio**

564 Denote the joint CDF of directional extreme wind speeds as  $H(v_1, v_2, \dots, v_{n_d})$   
565 where  $n_d$  is the total number of directions being partitioned. Such joint CDF can be

566 derived from the multivariate extreme value theory using a Gaussian Copula model,  
 567 which is expressed as (Zhang and Chen 2015; Luo and Huang 2016)

$$568 \quad H(v_1, v_2, \dots, v_{n_d}) = G_{n_d}(\Phi^{-1}[\Psi_{V_1}(v_1)], \Phi^{-1}[\Psi_{V_2}(v_2)], \dots, \Phi^{-1}[\Psi_{V_{n_d}}(v_{n_d})]) \quad (25)$$

569 where  $\Phi^{-1}$  is the inversed CDF of standard Gaussian distribution;  $G_{n_d}$  is the CDF of  
 570  $n_d$ -dimensional normal distribution with the zero mean and the covariance matrix  $\Sigma$  in  
 571 which  $\Sigma_{ii} = 1$  and  $\Sigma_{ij} = \Sigma_{ji} = E[\Phi^{-1}[\Psi_{V_i}(v_i)], \Phi^{-1}[\Psi_{V_j}(v_j)]]$ ; and  $\Psi_{V_i}(v_i)$  (  
 572  $i = 1, 2, \dots, n_d$ ) is the CDF of annual maximum wind speed in the  $i$  th direction. It  
 573 is proper to adopt the Gumbel distribution in Eq. (9) to model the annual maximum  
 574 wind speed in any direction. Hence, the CDF of the annual maximum can be  
 575 determined from that of monthly maximum following Eq. (11). It should be noted that  
 576 the Gaussian copula is equivalent to the Nataf transformation: both relate the non-  
 577 Gaussian variables to the Gaussian counterparts and can be united under the well-  
 578 known multivariate Gaussian translation theory (Grigoriu 2007). The extreme wind  
 579 speeds for 50 and 500 -year return period in each direction are plotted in Figure 12. It  
 580 can be observed that N and NW are two dominant directions in terms of the  
 581 magnitude of the extreme wind speed.

582 In engineering practice and in the insurance industry, the mean damage ratio is  
 583 often of primary concern. The mean damage ratio for a component such as steel  
 584 roofing can be treated as a function of the mean wind speed from the  $i$  th direction.  
 585 Alternatively, the mean wind speed  $v_i^d$ , producing a given damage level  $d$  in that  
 586 direction, can be obtained from Figure 10 (a). Therefore, for a component subjected to  
 587 wind loads from all directions, the probability not exceeding the damage level  $d$  can

588 then be calculated as

589 
$$P(D \leq d) = H(v_1^d, v_2^d, \dots, v_{n_d}^d) \quad (26)$$

590 If the directional extreme wind speeds can be assumed to be mutually independent,  
591 the estimation by Eq. (26) can be replaced by

592 
$$P(D \leq d) = \prod_{i=1}^{n_d} \Psi_{V_i}(v_i^d) \quad (27)$$

593 The damage of the steel roofing for  $Y$ -year return period,  $d_Y$ , can then be determined  
594 from

595 
$$Y = 1 / [1 - P(D \leq d_Y)] \quad (28)$$

596 The probabilities for various damage levels are illustrated in Figure 13, where the  
597 roofing damages considering wind directionality and those in 8 directions are  
598 included. It can be seen NW direction (7 th) retains the dominance among 8 directions  
599 due to the larger extreme wind speed and the higher damage risk in this direction. In  
600 contrast, another dominant N direction (8 th) has less influence in terms of extreme  
601 wind speed due to the lower damage risk. Besides, the consideration of wind  
602 directionality effect produces a larger damage estimation compared with those in 8  
603 individual directions. This is attributed to the fact that  
604  $H(v_1^d, v_2^d, \dots, v_{n_d}^d) \leq \min[\Psi_{V_i}(v_i^d)]$ . Furthermore, the directional extreme wind speeds  
605 are shown to be mutually independent, as seen in the almost identical estimations by  
606 Eqs. (26) and (27). This can be attributed to a dominant NW direction and low  
607 correlations among extreme wind speeds across different directions.

608 The aforementioned approach provides the estimation of the roofing damage  
609 where the variation of the damage ratio is not considered. If the mean damage ratio is

610 treated as a principle index in damage estimation, this approach will be quite  
 611 convenient to deal with the wind directionality. Otherwise, the variations of damage  
 612 ratio should be incorporated, which is discussed in the next subsection.

## 613 **8.2 With consideration of variation of damage ratio**

614 According to Huang et al. (2016), the STD of the damage ratio is larger when the  
 615 wind loading has a stronger correlation. This variation around the mean damage ratio  
 616 causes additional risk, which is sometimes termed as “secondary uncertainty”.  
 617 Ignoring the influence of the secondary uncertainty may result in an inadequate  
 618 assessment of the risk. The following discussions address the issue of quantifying the  
 619 damage considering the variation of damage ratio.

620 The probability of  $D$  not exceeding damage level  $d$  in all directions can be  
 621 expressed as

$$622 \quad P(D \leq d) = \int \cdots \int F_{D_1, D_2, \dots, D_{n_d}}(d|v_1, d|v_2, \dots, d|v_{n_d}) h(v_1, v_2, \dots, v_{n_d}) dv_1 dv_2 \cdots dv_{n_d} \quad (29)$$

623 where  $F_{D_1, D_2, \dots, D_{n_d}}(d_1|v_1, d_2|v_2, \dots, d_{n_d}|v_{n_d})$  is the joint CDF of damage ratios  
 624 conditioned on extreme wind speed  $v_i$  ( $i = 1, 2, \dots, n_d$ ). If the roofing damage is  
 625 mutually independent across directions, Eq. (29) becomes

$$626 \quad P(D \leq d) = \int \cdots \int \prod_{i=1}^{n_d} F_{D_i}(d|v_i) h(v_1, v_2, \dots, v_{n_d}) dv_1 dv_2 \cdots dv_{n_d} \quad (30)$$

627 where  $F_{D_i}(d|v_i)$  is the CDF of damage ratio in  $i$  th direction under  $v_i$ , which is served  
 628 as a complimentary fragility and obeys exceeding lognormal distribution (Lee and  
 629 Rosowsky 2005). If the directional extreme wind speeds are mutually independent,  
 630 which is the particular case for present study, the above formula can be approximated  
 631 by

632 
$$P(D \leq d) = \prod_{i=1}^{n_d} \int F_{D|i,v}(d) \psi_{V_i}(v) dv \quad (31)$$

633 where  $\psi_{V_i}(v)$  is the PDF of extreme wind speed in the  $i$  th direction.

634 Numerical results show that damage ratios across directions are almost  
635 independent, which can be explained by the fact that both the peak force and  
636 resistance on a fastener are independent for different directions. Hence, Eq. (31) can  
637 be used to estimate the damage. The result considering the damage ratio variation is  
638 plotted in Figure 13. It is clearly seen that this yields an estimation of a higher damage  
639 level in a certain return period (e.g., 50-year). That is, the consideration of damage  
640 variation leads to a larger risk for roofing claddings.

## 641 **9. Conclusions**

642 The paper presents an integrated damage estimation method for steel roofing  
643 cladding in high winds. In this method, both the wind loading correlation and wind  
644 directionality effects are incorporated. For illustration, the high-strength trapezoidal  
645 steel cladding is chosen as the roof sheathing which is connected to building frame by  
646 screws. The wind loading is derived from the wind pressure data from a wind tunnel.  
647 Some observations and conclusions are given as follows. (1) POD is a useful tool to  
648 interpolate wind pressure for the position where the pressure tap is not assigned in the  
649 wind tunnel test. (2) The internal pressure can be satisfactorily simulated by current  
650 methods. (3) The internal force on the fastener can be computed efficiently by the  
651 influence-surface method and its peak value can be estimated conveniently via  
652 Gumbel conversion method. (4) The failure probability and damage ratio can be  
653 estimated by Nataf transformation -based MCS accurately when the wind loading

654 correlation is considered. Results show that the wind loading correlation may  
655 noticeably increase the variation of the cladding damage. (5) The wind directionality  
656 is incorporated into damage estimations in this study. Methods for consideration of  
657 mean damage ratio and the variation of damage ratio are developed. Results show that  
658 the wind directionality may lead to a larger damage risk for claddings in high winds  
659 and its consideration will provide a reliability-consistent solution in risk management.

660 Moreover, the presented damage estimation framework for the low-rise building  
661 roof can be a useful tool in making damage assessments for new or existing buildings.  
662 Furthermore, the method may benefit the performance-based design for the low-rise  
663 buildings (e.g., Ciampoli et al. 2011).

664 It should be noted that the proposed framework may not be directly used to other  
665 cladding types, like standing-seam clipped cladding. Appropriate modifications  
666 should be made to apply this framework, especially in determinations of wind loads  
667 on cladding, and the failure mechanisms and influence functions at the connections.  
668 Hence, it would be worthwhile to apply the framework to consider different roof types  
669 and failure modes in future work.

670 **Appendix** Derivation the relation between correlations for peak wind pressures over 1  
671 and 10 min

672 The very long wind pressure data used to derive the relation between correlations  
673 for peak wind pressures over  $T_1 = 1$  min and  $T = 10$  min were obtained from  
674 Boundary Layer Wind Tunnel II at UWO. Two 1:50 scale house models, FL27 and  
675 FL30, located in the suburban terrain under different AOAs and surroundings were

676 tested. The sampling frequency for model scale is 400 Hz and the sampling time for  
677 model scale is 3 h. Based on the assumption that a full-scale mean wind speed at 10 m  
678 height in suburban exposure is 31.7 m/s, equivalent to a mean wind speed = 24.2 m/s  
679 at the mean roof height of 4 m (The mean roof heights of both houses are roughly 4  
680 m), the velocity scale is 1:5, the sampling frequency and time in full scale are 40 Hz  
681 and 30 h, respectively. More details can be found in Peng et al. (2014).

682 For each tap, the very long data (30 h) are divided into 1800 segments of 1-min  
683 duration and 180 segments of 10-min duration in the following analysis. Correlation  
684 coefficients among peak pressure coefficients over 1 min and 10 min are estimated for  
685 all test conditions. Because the sampling frequency and time in full scale vary with  
686 the different mean wind speed, these variations may influence the correlation of peak  
687 values. Thus correlation coefficients under mean wind speeds of 12.1 and 36.3 m/s at  
688 the roof height are also investigated. Figure 14 shows the relationship between  
689 correlation coefficients over two time intervals for two test conditions (FL27, 120°,  
690 isolated and FL30, 130°, surrounded) under three different mean wind speeds, where  
691  $\rho_T$  and  $\rho_{T_1}$  are correlation coefficients for peak values over  $T$  and  $T_1$  min. It can be  
692 seen that the relationships are similar for different building models, AOAs,  
693 surroundings and mean wind speeds.

694 The relationship between correlation coefficients of peak values over 1 min and  
695 10 min is fitted by the following polynomial

$$696 \quad \rho_T = \sum_{i=0}^4 a_i \rho_{T_1}^i \quad (32)$$

697 where the coefficients  $a_i$  for  $i = 0$  to 4 are determined as 0.007, 0.241, -0.232, 1.716

698 and -0.741, respectively. Although the uncertainties in the lower correlation for peak  
699 values are large, they should not have the significant effect on the roof damage  
700 estimation and can be neglected for simplicity.

## 701 **Acknowledgments**

702 The support from the National Natural Science Foundation of China (Grant No.  
703 51778546) and Youth Fund Program of Sichuan Province (2016JQ0005) is greatly  
704 acknowledged.

## 705 **Reference**

706 ASCE. (2010). Minimum design loads for buildings and other structures. ASCE7-10,  
707 Reston, VA.

708 Bienkiewicz, B., Ham, H. J., and Sun, Y. (1993). Proper orthogonal decomposition of  
709 roof pressure. *J. Wind Eng. Ind. Aerodyn.*, 50, 193-202.

710 Chen, Y., Kopp, G. A., and Surry, D. (2002). Interpolation of wind-induced pressure  
711 time series with an artificial neural network. *J. Wind Eng. Ind. Aerodyn.*, 90(02), 589-  
712 615.

713 Chen, Y., Kopp, G.A., and Surry, D. (2004). Spatial extrapolation of pressure time  
714 series on low buildings using proper orthogonal decomposition, *Wind Struct.*, 7, 373-  
715 392.

716 Ciampoli, M., Petrini, F., and Augusti, G. (2011). Performance-based wind  
717 engineering: towards a general procedure. *Struct. Safety*, 33(6), 367-378.

718 Cook, N. J., and Mayne, J. R. (1980). A refined working approach to the assessment  
719 of wind loads for equivalent static design. *J. Wind Eng. Ind. Aerodyn.*, 6(1-2), 125-

720 137.

721 Cope, A. D., Gurley, K. R., Gioffre, M., and Reinhold, T. A. (2005). Low-rise gable  
722 roof wind loads: Characterization and stochastic simulation. *J. Wind Eng. Ind.*  
723 *Aerodyn.*, 93(9), 719-738.

724 Dabral, A., and Ewing, B. T. (2009). Analysis of wind-induced economic losses  
725 resulting from roof damage to a metal building. *J. Business Val. Econ. Loss Anal.*,  
726 4(2).

727 Gavanski, E., Gurley, K. R., and Kopp, G. A. (2016). Uncertainties in the Estimation  
728 of Local Peak Pressures on Low-Rise Buildings by Using the Gumbel Distribution  
729 Fitting Approach. *J. Struct. Eng.*, 142(11), 04016106.

730 Ginger, J. D., Henderson, D. J., Leitch, C. J., and Boughton, G. N. (2007). Tropical  
731 cyclone larry: estimation of wind field and assessment of building damage. *Australian*  
732 *J. Struct. Eng.*, 7(3), 209-224.

733 Grigoriu, M., (2007). Multivariate distributions with specified marginals:  
734 Applications to wind engineering. *J. Eng. Mech.*, 133(2), 174–184.

735 Henderson, D. J. (2010). Response of pierced fixed metal roof cladding to fluctuating  
736 wind loads. Ph.D Dissertation, James Cook University.

737 Henderson, D. J., and Ginger, J. D. (2011). Response of pierced fixed corrugated steel  
738 roofing systems subjected to wind loads. *Eng. Struct.*, 33(12), 3290-3298.

739 Ho, T. C. E., Surry, D., Morrish, D., and Kopp, G. A. (2005). The UWO contribution  
740 to the NIST aerodynamic database for wind loads on low buildings: Part 1. Archiving  
741 format and basic aerodynamic data. *J. Wind Eng. Ind. Aerodyn.*, 93(1), 1-30.

742 Holmes, J. D., (1979). Mean and fluctuating internal pressures induced by wind. Proc.  
743 5<sup>th</sup> Intl. Conf. on Wind Eng. 435-440., Fort Collins, Colorado, USA.

744 Holmes, J. D., and Cochran, L. S. (2003). Probability distributions of extreme  
745 pressure coefficients. *J. Wind Eng. Ind. Aerodyn.*, 91(7), 893-901.

746 Holmes, J. D., and Ginger, J. D. (2012). Internal pressures – the dominant windward  
747 opening case – a review. *J. Wind Eng. Ind. Aerodyn.*, 100(1), 70-76.

748 Huang, G. (2008). Probabilistic analysis of load effects on tall buildings under  
749 stationary and nonstationary extreme winds. Ph.D Dissertation, Texas Tech  
750 University.

751 Huang, G., He, H., Mehta, K. C., and Liu, X. (2015). Data-based probabilistic damage  
752 estimation for asphalt shingle roofing. *J. Struct. Eng.*, 141(12), 04015065.

753 Huang, G., Ji, X., Luo, Y., and Gurley, K. R. (2016). Damage estimation of roof  
754 panels considering wind loading correlation. *J. Wind Eng. Ind. Aerodyn.*, 155, 141-  
755 148.

756 Jeong, S. H., Bienkiewicz, B., and Ham, H. J. (2000). Proper orthogonal  
757 decomposition of building wind pressure specified at non-uniformly distributed  
758 pressure taps. *J. Wind Eng. Ind. Aerodyn.*, 87(1), 1-14.

759 Konthesingha, K. M. C., Stewart, M. G., Ryan, P., Ginger, J., and Henderson, D.  
760 (2015). Reliability based vulnerability modelling of metal-clad industrial buildings to  
761 extreme wind loading for cyclonic regions. *J. Wind Eng. Ind. Aerodyn.*, 147, 176-185.

762 Laboy-Rodríguez, S.T., Gurley, K. R., and Masters, F. J. (2014). Revisiting the  
763 directionality factor in ASCE 7. *J. Wind Eng. Ind. Aerodyn.*, 133(4), 225–233.

764 Luo, Y., and Huang, G. (2016). Characterizing dependence of extreme wind  
765 pressures. *J. Struct. Eng.*, 10.1061/(ASCE)ST.1943-541X.0001699, 04016208.

766 Kopp, G.A. (2013). Wind Loads on Building Components and Cladding. *Advanced*  
767 *Structural Wind Engineering* (ed. Tamura, Y. & Kareem, A.), Springer, Tokyo, 177-  
768 195.

769 Lee, K. H., and Rosowsky, D. V. (2005). Fragility assessment for roof sheathing  
770 failure in high wind regions. *Eng. Struct.*, 27(6), 857-868.

771 Li, Y., and Ellingwood, B. R. (2006). Hurricane damage to residential construction in  
772 the us: importance of uncertainty modeling in risk assessment. *Eng. Struct.*, 28(7),  
773 1009-1018.

774 Liu, P. L., and Der Kiureghian, A. (1986). Multivariate distribution models with  
775 prescribed marginals and covariances. *Prob. Eng. Mech.*, 1(2), 105-112.

776 Luo, Y, and Huang, G. (2016). “Characterizing dependence of extreme wind  
777 pressures.” *J. Struct. Eng.* (ASCE), 10.1061/(ASCE)ST.1943-541X.0001699,  
778 04016208.

779 Mahendran, M. (1990). Fatigue behaviour of corrugated roofing under cyclic wind  
780 loading. *Civil Engineering Transaction, Institution of Engineers, Australia* 32(4), 219-  
781 226.

782 Mahaarachchi, D., and Mahendran, M. (2009). Wind uplift strength of trapezoidal  
783 steel cladding with closely spaced ribs. *J. Wind Eng. Ind. Aerodyn.*, 97(3), 140-150.

784 NIST (2006). Performance of physical structures in Hurricane Katrina and Hurricane  
785 Rita: A reconnaissance report. National Institute of Standards and Technology,

786 Gaithersburg, MD, USA

787 Oh, J. H., Kopp, G. A., and Inculet, D. R. (2007). The UWO contribution to the NIST  
788 aerodynamic database for wind loads on low buildings: Part 3. Internal pressures. *J.*  
789 *Wind Eng. Ind. Aerodyn.*, 95(8), 755-779.

790 Oh, J.H. and Kopp, G.A. (2014). Modelling of spatially and temporally-varying cavity  
791 pressures in air permeable, double-layer roof systems. *Building Environ.* 82, 135-150.

792 Peng, X., Yang, L., Gavanski, E., Gurley, K., and Prevatt, D. (2014). A comparison of  
793 methods to estimate peak wind loads on buildings. *J. Wind Eng. Ind. Aerodyn.*, 126,  
794 11-23.

795 Perry, D. C., McDonald, J. R., Saffir, H. S., and Asce, F. (1990). Performance of metal  
796 buildings in high winds. *J. Wind Eng. Ind. Aerodyn.*, 36, 985-999.

797 Simiu E., and Scanlan, R. H. (1996). *Wind Effects on Structures: Fundamentals and*  
798 *Applications to Design.* (Third edition), John Wiley & Sons, NY

799 Song F., and Ou J. (2009). Wind hazard damage estimation of industrial buildings. 7th  
800 Asia-Pacific Conf. on Wind Eng., Taipei, Taiwan, China.

801 St. Pierre, L.M., Kopp, G.A., Surry, D., and Ho, T.C.E. (2005). The UWO  
802 contribution to the NIST Aerodynamic database for wind loads on low buildings: Part  
803 2. Comparison of data with wind load provisions. *J. Wind Eng. Ind. Aerodyn.*, 93(1),  
804 31-59.

805 Tamura, Y., Ueda, H., Kikuchi, H., Hibi, K., Suganuma, S., and Bienkiewicz, B.  
806 (1997). Proper orthogonal decomposition study of approach wind-building pressure  
807 correlation. *J. Wind Eng. Ind. Aerodyn.*, 72, 421-431.

808 Vickery, B. J., and Bloxham, C. (1992). Internal pressure dynamics with a dominant  
809 opening. *J. Wind Eng. Ind. Aerodyn.*, 41(1-3), 193-204.

810 Xu, Y. L. (1995). Fatigue performance of screw-fastened light-gauge-steel roofing  
811 sheets. *J. Struct. Eng.*, 121(3), 389-398.

812 Xu, Y. L. (1997). Fatigue damage estimation of metal roof cladding subject to wind  
813 loading. *J. Wind Eng. Ind. Aerodyn.*, 72(1), 379-388.

814 Zhang, X., and Chen, X. (2015). Assessing probabilistic wind load effects via a  
815 multivariate extreme wind speed model: A unified framework to consider  
816 directionality and uncertainty. *J. Wind Eng. Ind. Aerodyn.*, 147, 30-42.

817 Zhao, M., and Gu M. (2011). Database-assisted wind vulnerability assessment for  
818 metal buildings. *Proc. 13<sup>th</sup> Intl. Conf. on Wind Eng.*, Amsterdam, Netherlands.

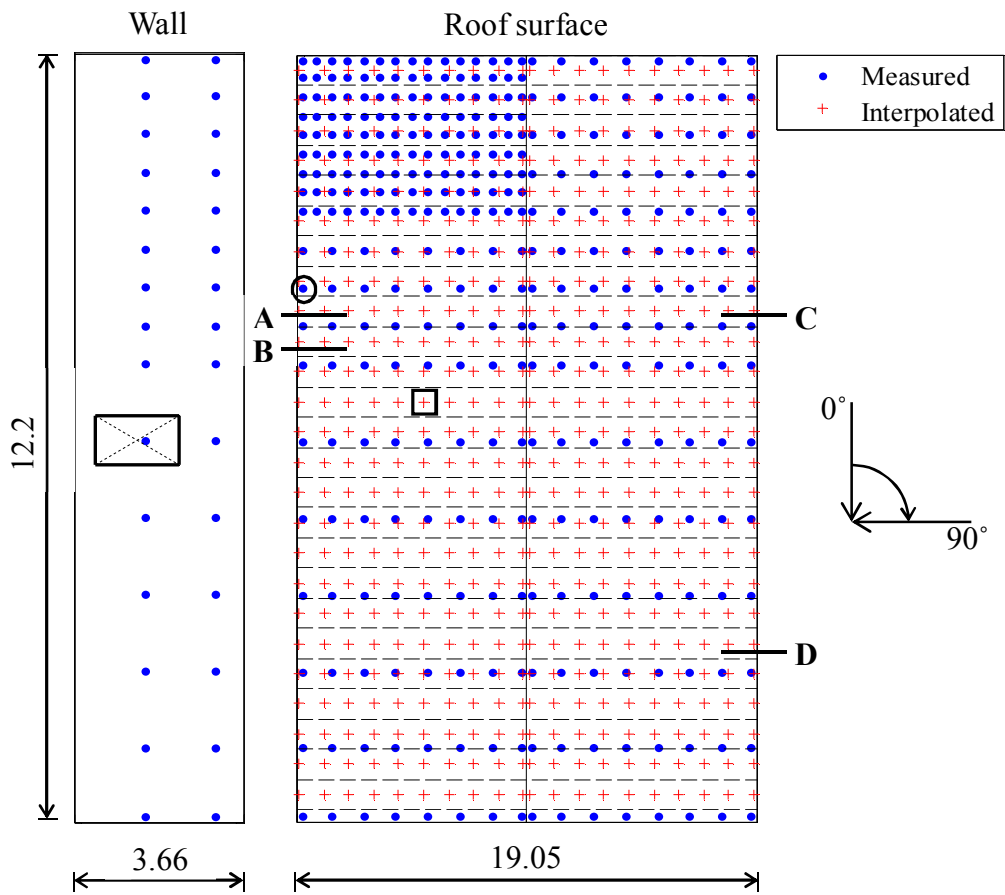
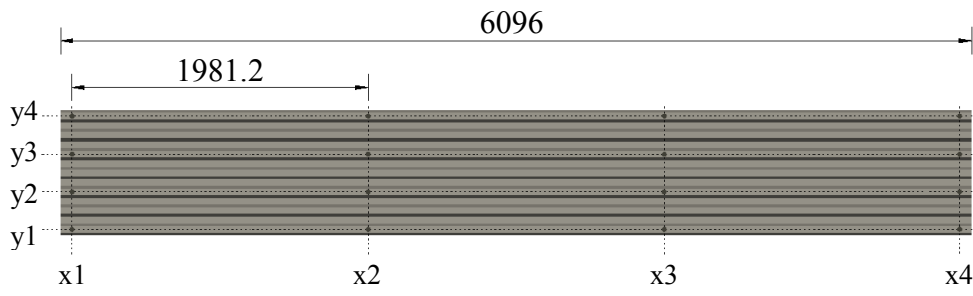
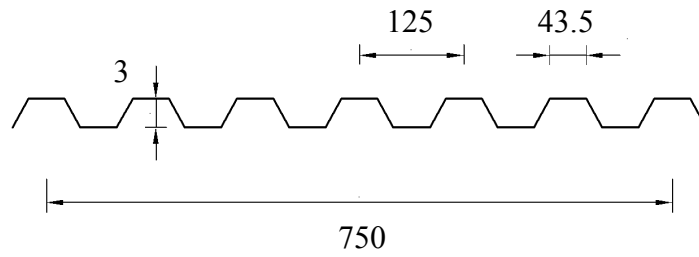


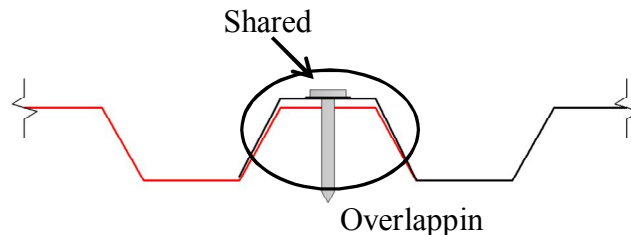
Figure 1 Tap locations and panel layout (Unit: m)



(a) Cladding configuration and screw distribution

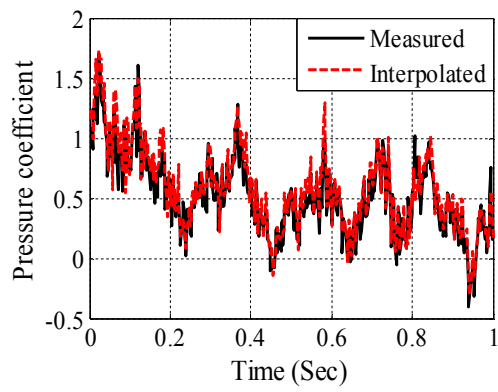


(b) Cross section

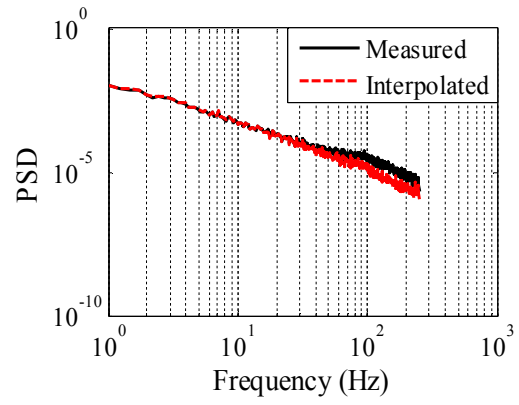


(c) Overlap

Figure 2 Configuration, dimension and joint type of cladding (Unit: mm)



(a) Time histories of fluctuations



(b) PSDs of fluctuations

Figure 3 Comparison of measured fluctuation and its interpolated counterpart at an existing tap (AOA of  $315^\circ$ )

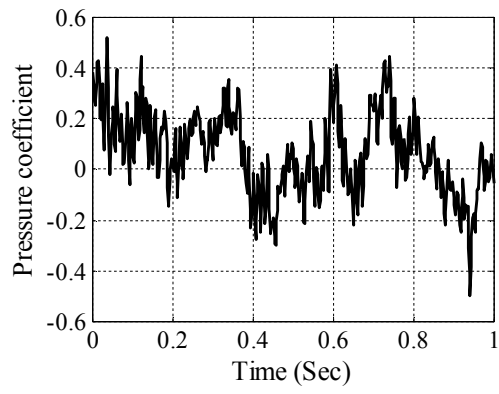
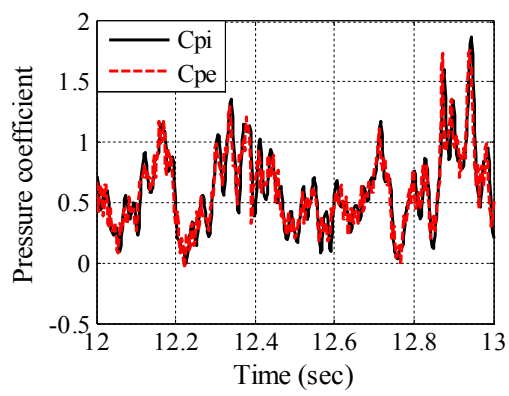
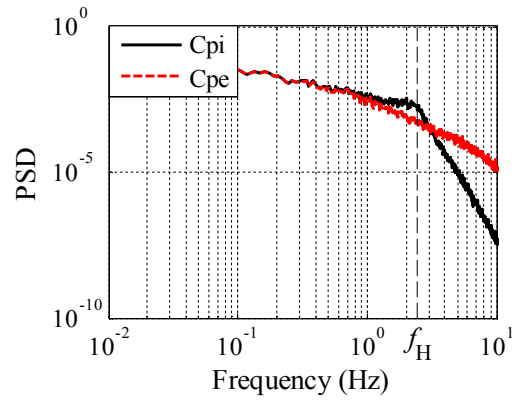


Figure 4 Interpolated fluctuation at a proxy tap (AOA of  $315^\circ$ )



(a) Time series



(b) PSD

Figure 5 Time series and spectra of internal and external pressure coefficients under wind speed of 37 m/s and AOA of  $315^\circ$

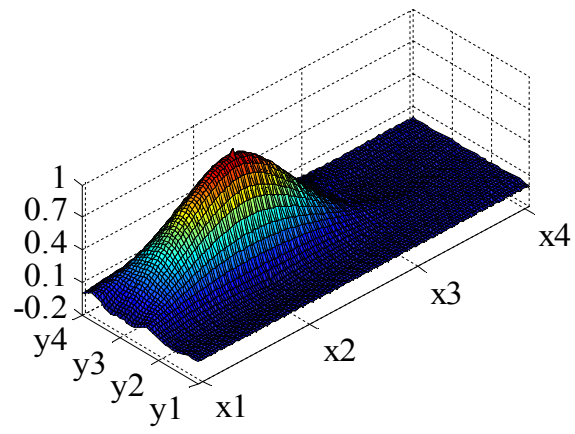


Figure 6 Influence surface for the internal force on screw x2y3

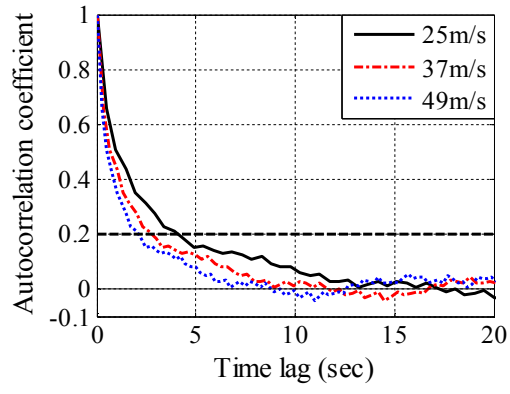


Figure 7 Autocorrelation coefficient of internal force at screw x2y2 on Cladding A

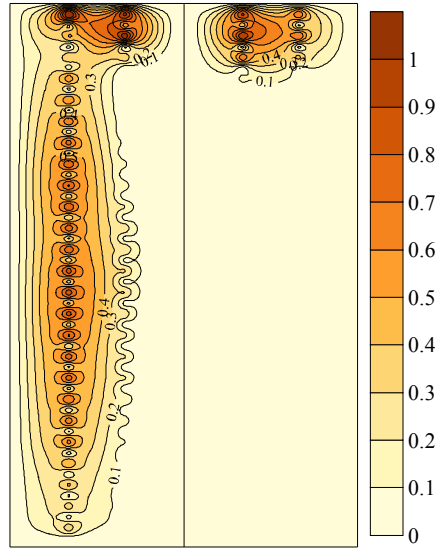
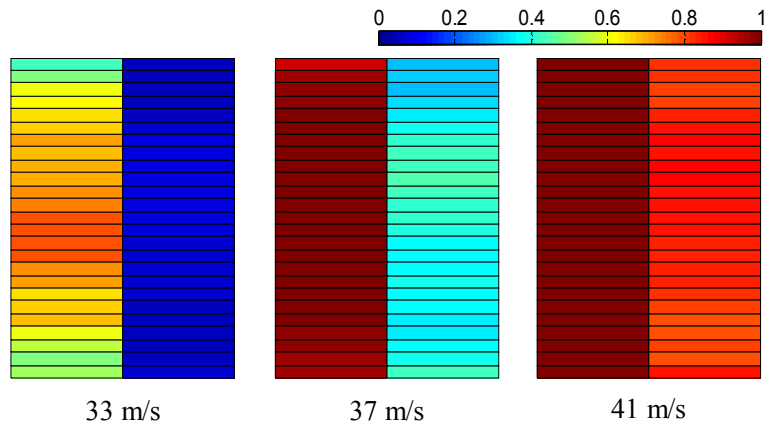
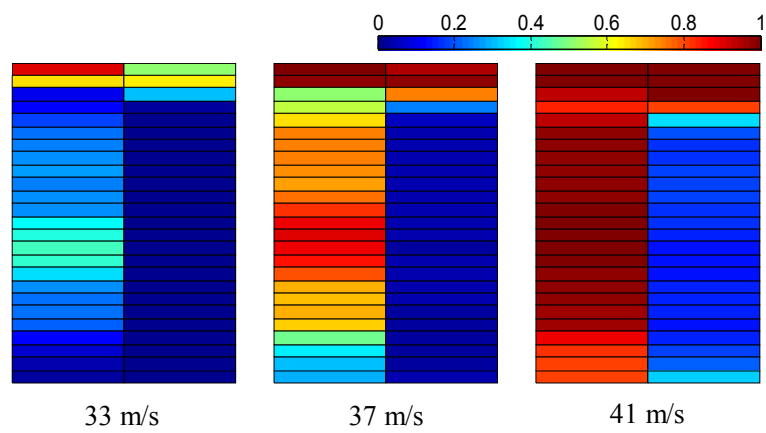


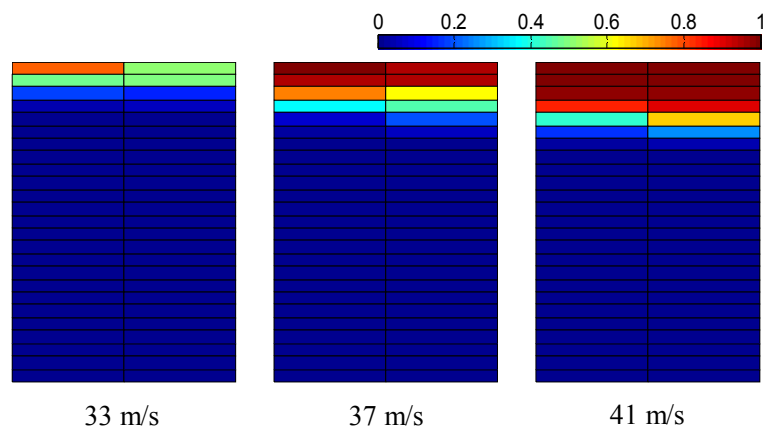
Figure 8 Failure probabilities for screws under speed of 37 m/s and AOA of 315°



(a) AOA of 270°

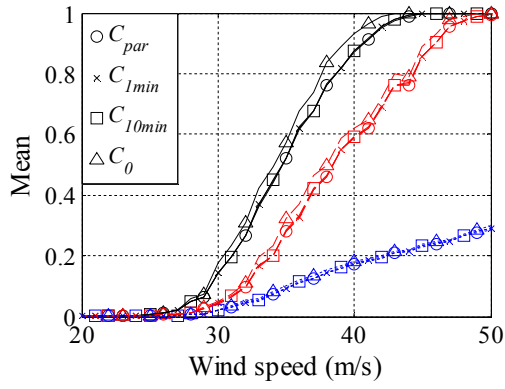


(b) AOA of 315°

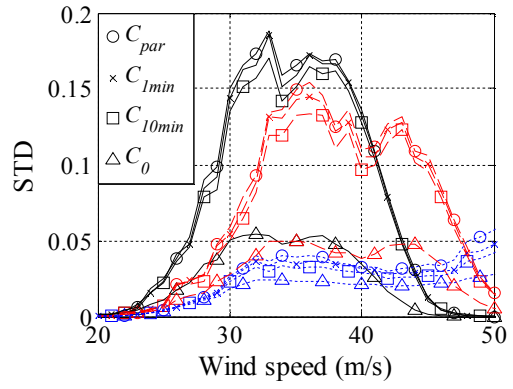


(c) AOA of 360°

Figure 9 Claddings failure probabilities under wind speeds of 33, 37 and 41 m/s, and AOA's of 270°, 315° and 360°



(a) Mean



(b) STD

Figure 10 Damage ratios for various wind speeds and AOAs (black solid line:  $270^\circ$ , red dash line:  $315^\circ$ , blue dot line:  $360^\circ$ )

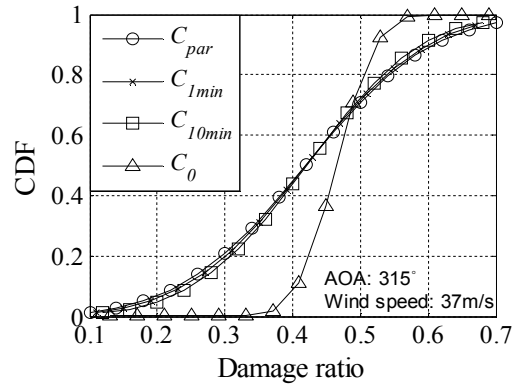


Figure 11 CDF of damage ratio under wind speed of 37 m/s and AOA of 315°

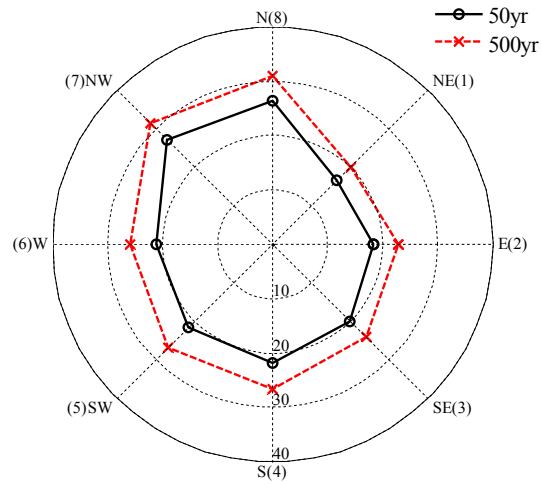


Figure 12 Extreme wind speeds for 50 and 500 –year return period (Unit: m/s)

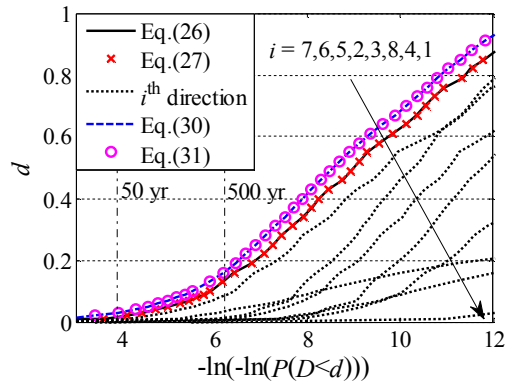
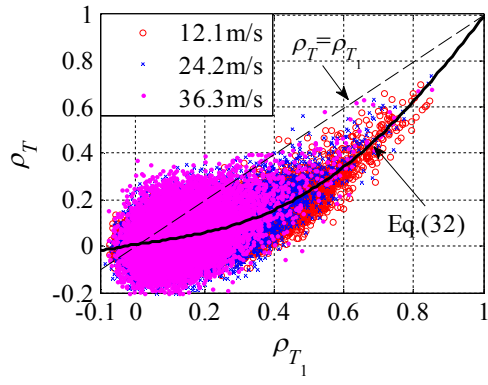
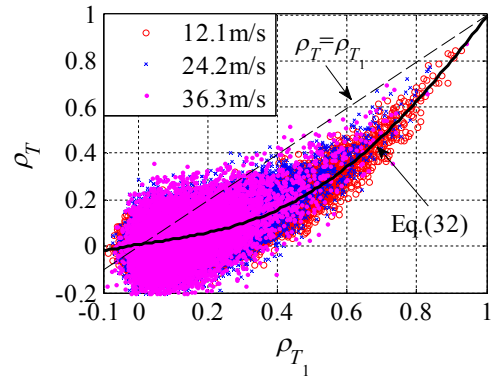


Figure 13 Estimations of roofing damage for various levels  $d$



(a) FL27,  $120^\circ$ , isolated



(b) FL30,  $130^\circ$ , surrounded

Figure 14 Correlation coefficients of peak pressure coefficients over  $T_1$  and  $T$

Table 1 Correlation coefficients among internal forces on selected screws (wind speed = 37 m/s and AOA = 315°)

Screw	x2y2 (Cladding A)	x3y2 (Cladding A)	x4y1 (Cladding B)	x2y4 (Cladding C)	x2y3 (Cladding D)
x2y2 (Cladding A)	1				
x3y2 (Cladding A)	0.956 0.896 0.794	1			
x4y1 (Cladding B)	0.910 0.837 0.688	0.957 0.891 0.785	1		
x2y4 (Cladding C)	0.920 0.855 0.720	0.952 0.811 0.645	0.979 0.930 0.856	1	
x2y3 (Cladding D)	0.917 0.877 0.760	0.945 0.806 0.637	0.956 0.846 0.704	0.962 0.937 0.870	1

Note: Numbers represent  $C_{par}$ ,  $C_{1min}$  and  $C_{10min}$  from top to bottom in a cell.